

10-2013

# On the Nonlinear Dynamics of Electromagnetically Transduced Microresonators

Andrew B. Sabater

*Birck Nanotechnology Center, Purdue University, [asabater@purdue.edu](mailto:asabater@purdue.edu)*

Vijay Kumar

*Birck Nanotechnology Center, Purdue University, [kumar2@purdue.edu](mailto:kumar2@purdue.edu)*

Aamer Mahmood

*Birck Nanotechnology Center, Purdue University, [amahmood@purdue.edu](mailto:amahmood@purdue.edu)*

Jeffrey F. Rhoads

*Birck Nanotechnology Center, Purdue University, [jfrhoads@purdue.edu](mailto:jfrhoads@purdue.edu)*

Follow this and additional works at: <http://docs.lib.purdue.edu/nanopub>

 Part of the [Nanoscience and Nanotechnology Commons](#)

---

Sabater, Andrew B.; Kumar, Vijay; Mahmood, Aamer; and Rhoads, Jeffrey F., "On the Nonlinear Dynamics of Electromagnetically Transduced Microresonators" (2013). *Birck and NCN Publications*. Paper 1496.  
<http://dx.doi.org/10.1109/JMEMS.2013.2257986>

This document has been made available through Purdue e-Pubs, a service of the Purdue University Libraries. Please contact [epubs@purdue.edu](mailto:epubs@purdue.edu) for additional information.

# On the Nonlinear Dynamics of Electromagnetically Transduced Microresonators

Andrew B. Sabater, *Student Member, ASME*, Vijay Kumar, *Student Member, ASME*, Aamer Mahmood, *Member, IEEE*, and Jeffrey F. Rhoads, *Member, ASME*

**Abstract**—This paper investigates the dynamics of electromagnetically actuated and sensed microresonators. These resonators consist of a silicon microcantilever and a current-carrying metallic wire loop. When placed in a permanent magnetic field and an alternating current is supplied, the devices vibrate due to Lorentz interactions. These vibrations, in turn, induce an electromotive force, which can be correlated to the dynamic response of the device. The nature of this transduction process results in an intrinsic coupling between the system's input and output, which must be analytically and experimentally characterized to fully understand the dynamics of the devices of interest. This paper seeks to address this need through the modeling, analysis, and experimental characterization of the nonlinear response of electromagnetically transduced microcantilevers in the presence of inductive and resistive coupling between the devices' input and output ports. A complete understanding of this behavior should enable the application of electromagnetically transduced microsystems in practical contexts ranging from resonant mass sensing to micromechanical signal processing. [2012-0223]

**Index Terms**—Electromagnetically transduced, input/output coupling, MEMS, nonlinear.

## I. INTRODUCTION

OVER THE PAST two decades, resonant MEMS devices have become an integral part of numerous technologies in the transportation, health, consumer electronics, and defense sectors. While MEMS devices can be actuated and sensed through a wide variety of mechanisms, this paper focuses on electromagnetic (also known as magnetomotive) transduction. In microscale contexts, electromagnetic transduction is appealing because it offers the benefits of scalability, self-sensing, and near-seamless integration with external electronics and associated hardware elements. These advantages render electromagnetically transduced microresonators suitable for a variety of applications, including mass sensing and micromechanical signal processing [1]–[8].

Manuscript received August 6, 2012; revised January 23, 2013; accepted April 3, 2013. Date of publication May 20, 2013; date of current version September 27, 2013. A preliminary version of this paper was presented at the 2012 ASME International Design Engineering Technical Conferences and Computers and Information in Engineering Conference, 6th International Conference on Micro- and Nanosystems. This work was supported in part by the National Science Foundation under Grant 0846385. Subject Editor G. K. Fedder.

The authors are with the School of Mechanical Engineering, Birck Nanotechnology Center and Ray W. Herrick Laboratories, Purdue University, West Lafayette, IN 47907 USA (e-mail: asabater@purdue.edu; kumar2@purdue.edu; amahmood@purdue.edu; jfrhoads@purdue.edu).

Color versions of one or more of the figures in this paper are available online at <http://ieeexplore.ieee.org>.

Digital Object Identifier 10.1109/JMEMS.2013.2257986

A majority of the electromagnetically actuated devices introduced to date consist of a compliant structural resonator with a current-carrying wire loop affixed to its surface (in some cases, the resonator itself acts as the current-carrying conductor). When placed in an external magnetic field, the flow of current through the wire loop induces a Lorentz force on the resonator, which results in mechanical motion. The movement of the current-carrying conductor through the external magnetic field, in turn, results in an induced electromotive force (EMF), which can be utilized for sensing purposes.

The microresonator detailed herein is similar in form to those previously introduced in [9]–[14]. The system consists of an electrically and mechanically isolated silicon microcantilever, which has two current loops (one for actuation and one for sensing) affixed to its surface. While this simplicity in physical design allows for high-yield device fabrication, the electromagnetic transduction approach introduces some complexity into the design due to the intrinsic coupling which exists between the input and output ports of the device. To minimize these coupling effects and achieve frequency separation between the input and output signals, many of the works detailed above exploited the dynamic behaviors of electromagnetically transduced devices which were parametrically excited [9]–[12]. In order to utilize such devices under direct excitation, the coupling between the input and output ports must be fully characterized. While input/output coupling mechanisms akin to those investigated here have been previously considered within the context of carbon nanotube and piezoelectric crystal resonators [15], [16], the present paper seeks to characterize the impact of these mechanisms on the dynamic response of electromagnetically transduced microresonators.

The paper begins in Section II with the modeling and subsequent analysis of the dynamic response of the electromagnetically transduced microresonators of interest, building, in part, upon the results of [17]. The work then continues in Section III with the development, and subsequent analysis of a model for the microresonators' induced EMF in the presence of coupling between the devices' input and output ports, due to both resistive and inductive sources. Section IV briefly describes the design and fabrication processes utilized for the electromagnetically transduced microresonators, and then proceeds with the experimental characterization of a representative device. Ultimately, the paper concludes with a brief summary and a discussion of current and future research directions.

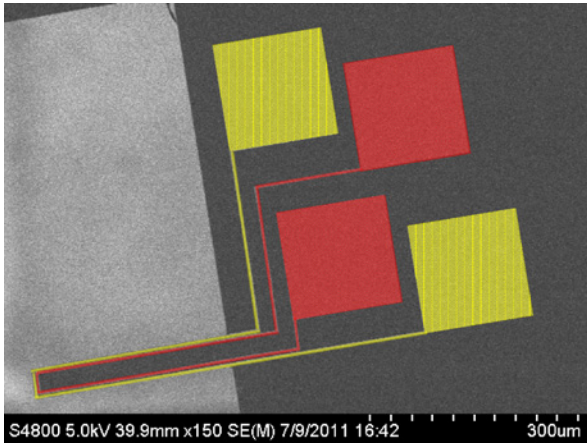


Fig. 1. Scanning electron micrograph of a representative electromagnetically transduced microresonator. The device consists of an electrically and mechanically isolated silicon microcantilever and two Au/Cr wire loops, which follow the perimeter of the microcantilever.

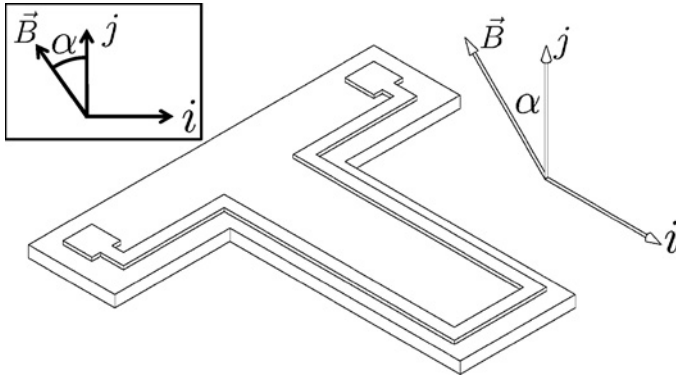


Fig. 2. Schematic diagram of the beam in three dimensions. As shown in the inset, the magnetic field  $\vec{B}$  is oriented at an angle  $\alpha$  with respect to the vertical reference. Note that only one of the two wire loops is depicted.

## II. DYNAMICS OF AN ELECTROMAGNETICALLY ACTUATED MICROBEAM

As previously noted and highlighted in Fig. 1, the devices of interest consist of an electrically and mechanically isolated microcantilever with two integrated Au/Cr wire loops, which is placed in a permanent magnetic field. To differentiate between the two wire loops in Fig. 1, the outer wire loop has been colored yellow and the inner loop has been colored red. Note that the magnetic field is oriented at an angle  $\alpha$  with respect to the vertical reference (Fig. 2), and, due to the scale of the device and the permanent magnet that is employed, the magnitude and direction of the field are assumed to be constant.

Assuming that the beam has a negligible rotational inertia, the specific Lagrangian  $\bar{L}$  of the device is defined as

$$\bar{L} = \frac{1}{2} \rho A [\dot{u}^2 + \dot{v}^2] - \frac{1}{2} EI \psi'^2 \quad (1)$$

where  $(\dot{\bullet})$  and  $(\bullet)'$  denote the derivatives with respect to time and the arc length variable  $s$ , respectively, and  $u$ ,  $v$ , and  $\psi$  are defined as in Fig. 3. Note that  $\rho$  is the mass density of the microbeam,  $A$  is the cross-sectional area,  $I$  is the undeformed

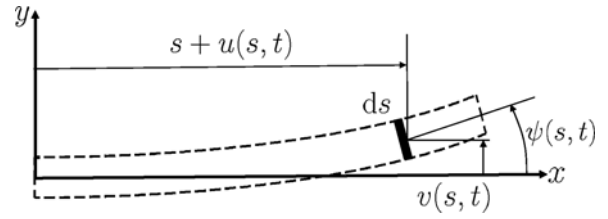


Fig. 3. Schematic diagram of the beam element and dynamic variables used for modeling. Note that  $u$ ,  $v$ , and  $\psi$  are the longitudinal, transverse and angular displacements of the differential beam element, respectively, and  $s$  is the arc length variable.

length,  $g$  is the width,  $E$  is the modulus of elasticity, and  $I$  is the cross-sectional moment of inertia.

The application of extended Hamilton's principle results in the following variational equation of motion for the system:

$$\begin{aligned} \delta H &= 0 \\ &= \delta \int_{t_1}^{t_2} \int_0^l \left\{ \bar{L} + \frac{1}{2} \lambda [1 - (1 + u')^2 - (v')^2] \right\} ds dt \\ &\quad + \int_{t_1}^{t_2} \int_0^l (Q_u \delta u + Q_v \delta v) ds dt \end{aligned} \quad (2)$$

where  $\lambda$  is a Lagrange multiplier used to enforce an inextensibility constraint and  $Q_u$  and  $Q_v$  are the nonconservative forces in the longitudinal and transverse directions, respectively. The longitudinal and transverse components of the Lorentz force are assumed to be point loads applied an infinitesimally small distance from the tip of the beam, such that the nonconservative forces do not need to be included in the boundary conditions. There is an additional force contribution in the transverse direction attributable to viscous damping. Note that  $c$  represents the specific viscous damping coefficient.

Integrating (2) successively by parts yields the two equations that govern the longitudinal and transverse vibrations of the system. While the details of this step have been excluded here for the sake of brevity, similar derivations can be found in [18] and [19]. Utilizing third-order Taylor's series expansions for  $u$  and  $\psi$ , an approximate solution for the Lagrange multiplier  $\lambda$  can be found, and subsequently used to reduce the two equations to a single equation which governs the transverse vibrations of the system. Nondimensionalizing the variables in the model, such that

$$\hat{v} = \frac{v}{v_0}, \quad \hat{s} = \frac{s}{l}, \quad \hat{t} = \frac{t}{T} \quad (3)$$

where  $v_0$  is the beam's thickness, and

$$T = \sqrt{\frac{\rho A l^4}{EI}}, \quad \hat{c} = \frac{cT}{\rho A} \quad (4)$$

yields a distributed-parameter model for the system. To study the dynamics of the system near the primary resonance, the distributed-parameter model can be reduced to an ordinary differential equation via modal projection. Introducing a single-mode expansion of the form

$$\hat{v}(\hat{s}, \hat{t}) = z(\hat{t}) \Psi(\hat{s}) \quad (5)$$

where  $\Psi$  is the first mode shape of an ideal cantilever and  $z$  is the displacement in the first mode, projecting the result onto

TABLE I  
DEFINITIONS OF THE NONDIMENSIONAL PARAMETERS USED IN (6)

$$\begin{aligned}
 \omega_0^2 &= \int_0^1 \Psi \Psi^{iv} d\hat{s} \\
 \tau &= \omega_0 \hat{t} \\
 (\bullet)' &= \frac{\partial(\bullet)}{\partial \tau} \\
 \epsilon k_3 &= \frac{v_0^2}{l^2 \omega_0^2} \left( 4 \int_0^1 \Psi \Psi' \Psi'' \Psi''' d\hat{s} + \int_0^1 \Psi \Psi''^3 d\hat{s} \right. \\
 &\quad \left. + \int_0^1 \Psi \Psi'^2 \Psi^{iv} d\hat{s} \right) \\
 \epsilon \lambda_1 &= \frac{g B l^2 \cos \alpha}{E I \omega_0^2} \int_0^1 \Psi'^2 d\hat{s} \\
 \epsilon \lambda_3 &= \frac{v_0^2 g B \cos \alpha}{2 E I \omega_0^2} \int_0^1 \Psi'^4 d\hat{s} \\
 \epsilon \beta &= \frac{v_0^2}{l^2} \left( \int_0^1 \Psi \Psi'' \int_1^{\hat{s}} \int_0^{\hat{s}_2} \Psi'^2 d\hat{s}_1 d\hat{s}_2 d\hat{s} \right. \\
 &\quad \left. + \int_0^1 \Psi \Psi' \int_0^{\hat{s}} \Psi'^2 d\hat{s}_1 d\hat{s} \right) \\
 \epsilon \eta_1 &= \frac{g B l^3 \sin \alpha}{E I v_0 \omega_0^2} \Psi|_{\hat{s}=1}
 \end{aligned}$$

the first mode shape, and rescaling the time variable (again) yields the final lumped-parameter equation of motion for the system

$$\begin{aligned}
 z'' + \frac{\epsilon}{Q} z' + [1 + \epsilon \lambda_1 i(\tau)] z + [\epsilon k_3 + \epsilon \lambda_3 i(\tau)] z^3 \\
 + \epsilon \beta (z z'^2 + z^2 z'') = \epsilon \eta_1 i(\tau). \quad (6)
 \end{aligned}$$

Here,  $Q$  represents the resonator's quality factor,  $i(\tau)$  is the excitation current, and  $\epsilon$  is a bookkeeping parameter introduced to facilitate analysis. The remainder of the parameters included here are defined in Table I. Note that a second dimensionless time scale  $\tau$  has been introduced here such that the natural frequency of (6) is close to unity. This time scale is used instead of the first dimensionless time scale  $\hat{t}$ , as the natural frequency of the equation of motion using the first dimensionless time scale is  $\omega_0$ , which itself is dependent on the boundary conditions of the microbeam.

Assuming all parameters with an  $\epsilon$  scaling in (6) are sufficiently small, the method of averaging can be used to generate the frequency response of the resonator. Employing the following coordinate transformation:

$$\begin{aligned}
 z(\tau) &= a(\tau) \cos[\tau + \phi(\tau)], \\
 z'(\tau) &= -a(\tau) \sin[\tau + \phi(\tau)] \quad (7)
 \end{aligned}$$

assuming that the excitation current is at a single frequency  $\Omega$

$$i(\tau) = i_0 \cos \Omega \tau \quad (8)$$

and introducing a detuning parameter to characterize the difference between the natural frequency of the microbeam and the excitation frequency

$$\epsilon \sigma = \Omega - 1 \quad (9)$$

the slow-flow equations are given by

$$\begin{aligned}
 a' &= -\frac{\epsilon}{2} \left[ \frac{a}{Q} + i_0 \eta_1 \sin(\phi - \epsilon \sigma \tau) \right] + O(\epsilon^2), \\
 a\phi' &= \frac{\epsilon}{8} [(3k_3 - 2\beta)a^3 - 4i_0 \eta_1 \cos(\phi - \epsilon \sigma \tau)] + O(\epsilon^2). \quad (10)
 \end{aligned}$$

To further simplify the slow-flow equations, two additional coordinate transformations of  $\hat{t} = \epsilon \tau$  and  $\theta = \phi - \epsilon \sigma \tau$  can be introduced. This yields

$$\begin{aligned}
 a' &= -\frac{1}{2} \left[ \frac{a}{Q} + i_0 \eta_1 \sin \theta \right], \\
 a\theta' &= \frac{1}{8} [(3k_3 - 2\beta)a^3 - 4i_0 \eta_1 \cos \theta - 8\sigma a]. \quad (11)
 \end{aligned}$$

Note that in (11), implicitly

$$(\bullet)' = \frac{\partial(\bullet)}{\partial \hat{t}} \quad (12)$$

and that  $a$  and  $\theta$  are functions of  $\hat{t}$ . By solving for the steady-state solutions of (11), a third-order polynomial equation that relates the displacement amplitude to the excitation frequency can be derived

$$16Q^2 i_0^2 \eta_1^2 = A [16 + Q^2 (\alpha_3 A - 8\sigma)^2] \quad (13)$$

where  $\alpha_3 = 3k_3 - 2\beta$  and  $a^2 = A$ . From this equation, it can be seen that the maximum amplitude is given by  $i_0 \eta_1 Q$ , and it occurs at  $\sigma = \alpha_3 i_0^2 \eta_1^2 Q^2 / 8$ . The threshold value of current corresponding to the onset of bistability ( $i_{cr}$ ) can be calculated by invoking the implicit function theorem

$$i_{cr} = \frac{4\sqrt{2}}{3^{3/4} Q^{3/2} \sqrt{|\alpha_3|} |\eta_1|}. \quad (14)$$

Note that below this critical value the response is single valued and stable, and above the critical current there exists a finite range of frequency where multiple steady-state solutions exist [20].

Using (13), the frequency response characteristics of the system can be investigated. Fig. 4 depicts the velocity of the resonator as a function of the excitation frequency, for a representative device with parameters given as shown in Table II. Here, the stable steady-state solutions are represented by dashed lines with long solid segments, while unstable solutions are denoted by dashed lines with short solid segments. Note that the quality factor employed here was selected to match experimental values obtained from frequency sweeps conducted within the linear response regime. Also, note that while the solutions to (13) are dependent on the supplied current, and the responses in Fig. 4 depend on the excitation voltage, in the following section a circuit model is presented which links these two quantities.

### III. INDUCED ELECTROMOTIVE FORCE

As noted earlier, the vibration of the microcantilever in a permanent magnetic field results in an induced EMF. As previously noted in [17], the induced EMF due to mechanical vibrations ( $V_{EMF}$ ) is approximated to third order by

$$V_{EMF} = \kappa_1 z' + \kappa_2 z z' \quad (15)$$

TABLE II  
DIMENSIONS AND MATERIAL PROPERTIES OF A REPRESENTATIVE  
ELECTROMAGNETICALLY ACTUATED MICROCANTILEVER

Physical Parameter	Value
Length of beam ( $l$ )	250 $\mu\text{m}$
Width ( $g$ )	50 $\mu\text{m}$
Thickness ( $v_0$ )	2 $\mu\text{m}$
Modulus of elasticity ( $E$ )	159 GPa
Mass density ( $\rho$ )	2330 $\text{kg/m}^3$
Magnetic field strength ( $B$ )	1 T
Magnetic field orientation ( $\alpha$ )	$\pi/3$ rad
Au/Cr trace resistance ( $R_{\text{Au/Cr}}$ )	30 $\Omega$
Quality factor ( $Q$ )	7100

Based on these values, the natural frequency is expected to be approximately 42.70 kHz. The quality factor was chosen to match the experimental values obtained from frequency sweeps conducted within the linear response regime.

where

$$\begin{aligned}\kappa_1 &= -\frac{Bg \sin \alpha v_0 \omega_0}{T} \frac{\int_0^1 \Psi \int_0^1 \Psi' d\hat{s} d\hat{s}}{\int_0^1 \Psi d\hat{s}}, \\ \kappa_2 &= \frac{Bg \cos \alpha v_0^2 \omega_0}{lT} \frac{\int_0^1 \Psi \int_0^1 \Psi'^2 d\hat{s} d\hat{s}}{\int_0^1 \Psi d\hat{s}}.\end{aligned}\quad (16)$$

An equivalent circuit, which describes the electrical coupling between the input and output of this device, is shown in Fig. 5. An excitation signal is provided by a voltage source  $V_{in}$ , which supplies a current  $i_{in}$  through the Thévenin equivalent resistance of the source  $R_s$  and a coaxial cable of resistance  $R_{Co}$ . Note that  $R_{Co}$  is henceforth assumed to be 50  $\Omega$  and that in an effort to minimize noise effects and the supplied current, the source output impedance  $R_s$  was set to 10 k $\Omega$  during experimentation. This current is then split into two components,  $i(\tau)$  flowing into the outer Au/Cr wire trace and another flowing through the resistor  $R_{Si}$ . This lumped resistor  $R_{Si}$  is used to describe several effects related to conduction between the inner and outer wires, including metal–semiconductor junctions formed by the contact pads and silicon substrate, which are assumed here to be ohmic contacts, and the finite resistivity of the silicon substrate. The induced EMF is included in the model as two current-controlled voltage sources in series with the lumped resistances for the Au/Cr wire traces, denoted as  $R_{\text{Au/Cr}}$ . The polarities of the voltage sources are opposite due to the polarity of the inner and outer wire traces being opposite. To account for the inductive coupling effects, which are primarily due to the probe station used for measurement and the contact pads, two inductors of self-inductance  $L$  and mutual inductance  $M$  are added in series with the coaxial cables used to actuate and sense the device. The resistor  $R_M$  is the input impedance of the lock-in amplifier used to acquire the measured voltage  $V_M$ . Since the input impedance of the lock-in amplifier used is nominally 10 M $\Omega$ , it is assumed that  $i_{out}$  is effectively zero. It is worth noting that in previous works [14], issues with inductive coupling have been accounted for and observed;

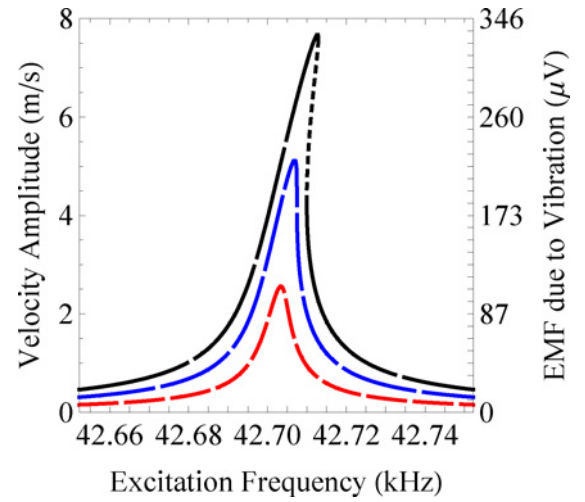


Fig. 4. Steady-state velocity amplitude plotted as a function of the excitation frequency for a device with dimensions and material properties given as shown in Table II. Note that in this figure, and in Figs. 6–8, the responses shown in red with short solid segments, blue with medium solid segments and black with long solid segments correspond to excitation voltages of 328 mV, 655 mV and 983 mV, respectively. The response shown in blue with medium solid segments corresponds to the onset of bistability. In the absence of inductive and resistive coupling between the input and output, the vertical axis on the right depicts the induced EMF. The results of these coupling effects is discussed in the following section.

however issues with resistive coupling have not been reported with electromagnetically transduced devices.

In regards to the lumped-parameter model of the mutual inductance between the transduction circuits, three factors have been identified that contribute to the measured value: the probe station, the contact pads, and the geometry of the Au/Cr wire traces. While all of these factors contribute to the mutual inductance, the relative influence of each of these sources is not the same. It is believed that the primary contributions to the mutual inductance are from the probe station and the contact pads, because in the absence of these factors, the mutual inductance would be several orders of magnitude less. Specifically, if the device was modified such that the probe station and contact pads were not needed, an estimate for the upper bound of the mutual inductance between the transduction circuits would be the self-inductance of a closed-loop wire trace of similar size, since as the spacing between the two wire traces decreases, the mutual inductance approaches the self-inductance (see [21] for methods to estimate self- and mutual inductance). This value is on the order of 1 nH, while the experimentally determined value is close to 10  $\mu\text{H}$ . Accordingly, with the current implementation of the device, the contributions of the wire geometry to the mutual inductance are largely insignificant. This, however, may not be true in integrated devices where a probe station is not needed.

To develop a simplified model for the measured voltage, it is assumed that the self-inductance of the outer wire loop  $L$  is small,  $R_{Si}$  is much larger than  $R_{\text{Au/Cr}}$  and that the induced EMF in the outer loop is small enough that the supplied current and the excitation voltage are in phase and are linearly related. Note that experimentally  $R_{Si}$  has been measured to be greater than 1 M $\Omega$ , however in cases where resistive coupling effects dominate the response, a  $R_{Si}$  as low as 1 k $\Omega$  has been

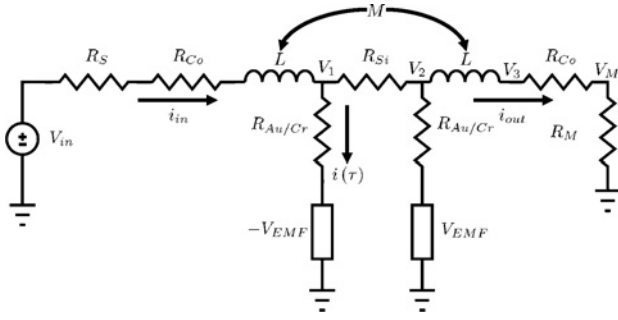


Fig. 5. Equivalent circuit diagram used to model the electrical coupling between the input and output ports of the presented device. An excitation signal is provided by a voltage source  $V_{in}$ , which supplies a current  $i_{in}$  through the Thévenin equivalent resistance of the source  $R_s$  and a coaxial cable of resistance  $R_{Co}$ . The inner and outer wire loops are modeled as resistors  $R_{Au/Cr}$  and the induced EMF is included as two current-controlled voltage sources. Note that the polarities of these sources are opposite due to the polarities of the inner and outer wire loops being opposite. To account for the conduction between the inner and outer wires, a lumped resistor  $R_{Si}$  is used. Effects related to inductive coupling are included with two inductors with self-inductance  $L$  and mutual inductance  $M$ . The resistor  $R_M$  is the input impedance of the lock-in amplifier used to acquire the measured voltage  $V_M$ . Note that  $R_{Si}$  is assumed to be very large such that  $i_{in} \approx i(\tau)$ ,  $R_M$  is assumed to be very large such that  $i_{out} \approx 0$  and the induced EMF in the outer wire trace does not influence the supplied current to the device.

observed. Accordingly, the current supplied to the device  $i_{in}$  is approximately equal to the current in the outer wire  $i(\tau)$ , or

$$i(\tau) = \frac{V_{in}}{R} \quad (17)$$

where  $R = R_s + R_{Co} + R_{Au/Cr}$ . As mentioned in the previous section, this is the relationship between the supplied current and the excitation voltage used in Fig. 4. Note that under these assumptions,  $V_{in} - V_1 = i(\tau)[R_s + R_{Co}]$ . By applying Kirchhoff's current law to the node where  $V_2$  is present and using the fundamental relationship between the current and voltage for an inductor, under the assumption that  $i_{out}$  is effectively zero, two additional equations are generated that can be used to solve for the measured voltage

$$\begin{aligned} \frac{V_1 - V_2}{R_{Si}} &= \frac{V_2 - V_{EMF}}{R_{Au/Cr}}, \\ V_2 - V_M &= -M \frac{\omega_0}{T} i'(\tau). \end{aligned} \quad (18)$$

These equations reveal that, under the stated assumptions, the measured voltage is effectively the superposition of three effects: the induced EMF due to the vibration of the microcantilever, the inductive coupling between the wire loops, and the resistive coupling due to conduction in the silicon of the microcantilever

$$V_M = c_1 V_{EMF}[i(\tau)] + c_2 V_{in}(\tau) + c_3 V'_{in}(\tau) \quad (19)$$

where

$$\begin{aligned} c_1 &= \frac{R_{Si}}{R_{Si} + R_{Au/Cr}}, \\ c_2 &= \frac{R_{Au/Cr}^2}{(R_{Si} + R_{Au/Cr})R}, \\ c_3 &= \frac{M\omega_0}{TR}. \end{aligned} \quad (20)$$

Note that for physically consistent systems,  $c_1$  is approximately one,  $c_2$  is nearly zero, and  $c_3$  is related to the mutual inductance, scaled to account for the nondimensionalized time.

Since the EMF is measured in experiments using a lock-in amplifier that is set to measure at the excitation frequency, higher order harmonics in the induced EMF due to vibration are filtered out. Thus, using the results from above

$$V_M = -c_1 \kappa_1 a \sin(\Omega\tau + \theta) + c_2 V_0 \cos(\Omega\tau) - c_3 V_0 \sin(\Omega\tau) \quad (21)$$

where  $V_0$  is the amplitude of the excitation voltage  $V_{in}$ . Equation (21) can be rewritten such that the amplitude and phase of the measured EMF can be easily identified

$$\begin{aligned} V_M &= a_m \cos[\Omega\tau + \theta_M], \\ a_M &= \sqrt{C_M^2 + S_M^2}, \\ C_M &= c_2 V_0 + \frac{c_1 \kappa_1 A R}{V_0 Q \eta_1}, \\ S_M &= -\left( \frac{c_1 \kappa_1 A R (A\alpha_3 - 8\sigma)}{4V_0 \eta_1} + c_3 V_0 \right), \\ \tan[\theta_M] &= \frac{Q(c_1 \kappa_1 A R (A\alpha_3 - 8\sigma) + 4c_3 \eta_1 V_0^2)}{4(c_1 \kappa_1 A R + c_2 \eta_1 Q V_0^2)}. \end{aligned} \quad (22)$$

When the quality factor is large and the effects of resistive coupling are small,  $C_M$  is effectively zero. Since the value of  $S_M$  can be positive and negative, it is possible that this term can equal zero, thus when inductive coupling is dominant, an *effective antiresonance* can be created. This antiresonance due to inductive coupling is in general observed at a specific frequency, however, a much broader antiresonance regime can be observed if resistive coupling is large, as the two terms in  $C_M$  are always of opposite sign. In addition, the equation for  $a_M$  predicts that the magnitude of the input voltage  $V_0$  biases the response such that nonresonant responses are nontrivial and are scaled in an approximately linear fashion by  $V_0$ . The phase response of (22) also predicts that the phase of the response in the nonresonant regime is dependent on the input/output coupling. For example, if the input and output are strongly inductively coupled, the phase of the nonresonant response will approach  $90^\circ$ , but if the input and output are strongly resistively coupled, the phase of the nonresonant response will approach  $0^\circ$ .

Though not necessarily obvious from (22), in the presented sensing configuration, where the positive excitation and sensing probes are placed on opposite sides of the microcantilever, strong resistive coupling can significantly degrade the amplitude of the response (note that  $\kappa_1/\eta_1 < 0$ ). It is also worth noting that in the absence of inductive and resistive coupling, the input and output are  $180^\circ$  out of phase at resonance. As such, reversing the polarity of the sensed voltage can exploit constructive interference in the response between the parasitic resistive coupling voltage and the induced EMF due to vibration, because at resonance the resistively coupled voltage and induced EMF due to vibration are in phase. Mathematically, reversing the polarity of the sensed voltage changes the sign of  $c_1$  and  $c_3$ , but not  $c_2$ . The authors acknowledge that polarity-dependent responses are unusual, but examples of polarity-dependent responses caused by parasitic effects



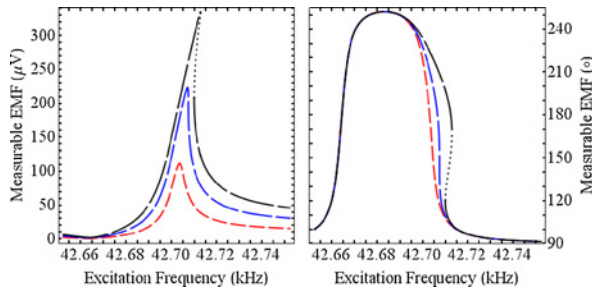


Fig. 6. Analytically predicted measurable EMF plotted as a function of the excitation frequency for a moderately low input coupling case where  $M = 1 \mu\text{H}$  and  $R_{Si} = 1 \text{ M}\Omega$ . The response is very similar to the one in Fig. 4, however the amplitude response contains an antiresonance and exhibits a response bias. In addition, the phase response approaches  $90^\circ$  for nonresonant responses due to the input/output coupling primarily being caused by inductive coupling.

can be found in the literature on transformers for integrated circuits, which have many similarities to the presented device [22], [23].

Figs. 6–8 depict the amplitude of the measurable EMF for the same excitation levels used in Fig. 4, with different values of the mutual inductance  $M$  and the silicon substrate resistance  $R_{Si}$ , and, in one case, the reversed polarity response. The same convention for classifying the excitation levels and stability used in Fig. 4 is employed. For the case shown in Fig. 6, where the effects of mutual inductance and resistive coupling are small, the amplitude response is very similar to those depicted in Fig. 4. Yet even in this case, the three distinct phenomena are demonstrated: an effective antiresonance, input voltage biased nonresonant responses, and the nonresonant phase response approaching a constant that is dependent on the input/output coupling. If the effects of inductive and resistive coupling are significantly increased, as in Fig. 7, then not only is the effect of the antiresonance increased, but the shape of the amplitude response is dramatically changed such that bistability of the response manifests in an amplitude response for a reverse frequency sweep sometimes being larger than the forward frequency sweep, even though the mechanical response is characterized as hardening. While it is predicted that effects related to inductive coupling can be mitigated with wire bonding, resistive coupling will still exist. Fig. 8 demonstrates how effective the reversed polarity configuration is at combating the effects related to resistive coupling. It is worth noting that the mutual inductance and silicon substrate resistances are the same in Figs. 7 and 8, yet the antiresonances are quenched and the signal return is increased.

Clearly, from the results presented here, input/output coupling significantly alters both the qualitative and quantitative nature of the measurable EMF signal, and thus must be accounted for in the course of predictive design. It is also important to note that due to the coupling between the input and output ports, broadband noise in the input can significantly degrade the signal-to-noise ratio associated with the device. Likewise, since the amplitude of the frequency response is nontrivial away from resonance, excitations at those frequencies are not filtered from the response.

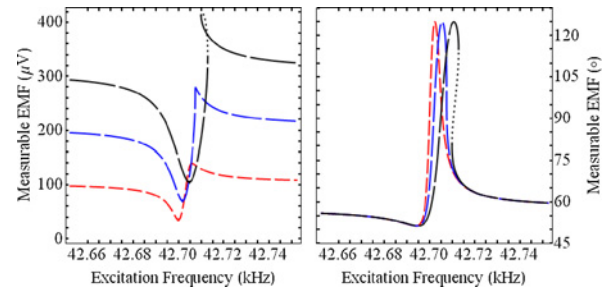


Fig. 7. Analytically predicted measurable EMF plotted as a function of the excitation frequency for a strong input coupling case where  $M = 10 \mu\text{H}$  and  $R_{Si} = 500 \Omega$ . In addition to an antiresonance and response bias, this response is an example of a case where the amplitude response of the reverse sweep is sometimes larger than the forward sweep, even though the mechanical response is characterized as hardening. Due to the inductive and resistive coupling effects being of similar magnitude, the phase response in the nonresonant response regime approaches a value between  $0^\circ$  and  $90^\circ$ .

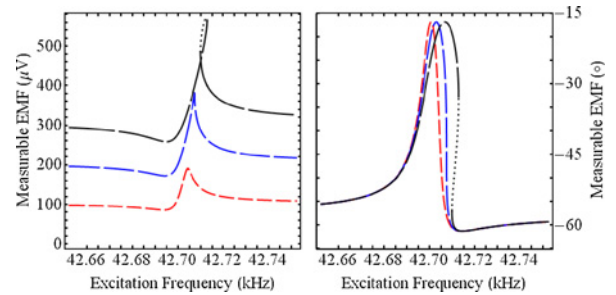


Fig. 8. Analytically predicted measurable EMF plotted as a function of the excitation frequency for a strong input coupling case where  $M = 10 \mu\text{H}$  and  $R_{Si} = 500 \Omega$ . Here the polarity of the measurable EMF is reversed. While response bias effects are still observed, the antiresonance is significantly reduced. While it is expected that inductive coupling issues could be reduced with wire bonding, resistive coupling effects will still be present. This method provides a means of exploiting resistive coupling for enhanced signal return.

#### IV. EXPERIMENTAL RESULTS

To validate the results presented in the previous section, a series of devices were fabricated at the Birck Nanotechnology Center using standard silicon-on-insulator (SOI) microfabrication processes (Fig. 9). The process used an SOI wafer, 4 inches in diameter. The device layer was p-type doped silicon with very high resistivity ( $>1000 \Omega \text{ cm}$ ) and was  $2 \mu\text{m}$  thick, the oxide layer was  $2 \mu\text{m}$  thick and the handle layer was  $500 \mu\text{m}$  thick. Wire loops were formed by evaporating Cr and Au on the surface and then using a lift-off process. The cantilevers were formed using reactive ion etching on the device layer. The oxide layer was exposed using deep reactive ion etching on the handle layer and then the devices were released using hydrofluoric acid.

To experimentally characterize the response of these devices, a Polytec MSA-400 laser Doppler vibrometer (LDV) was used in conjunction with a SUSS MicroTec PLV-50 vacuum probe station. Fig. 10 shows a part of the experimental setup used to study the optical response. The probe station consists of a vacuum chamber, whose pressure is controllable to a minimum set point of  $75 \mu\text{Torr}$ . The devices are placed in a permanent magnetic field with a field strength of approximately  $1 \text{ T}$  near the poles. The permanent magnet used for these experiments is a NdFeB slab magnet with dimensions  $2.5 \text{ cm} \times 2.5 \text{ cm} \times 0.25 \text{ cm}$ .

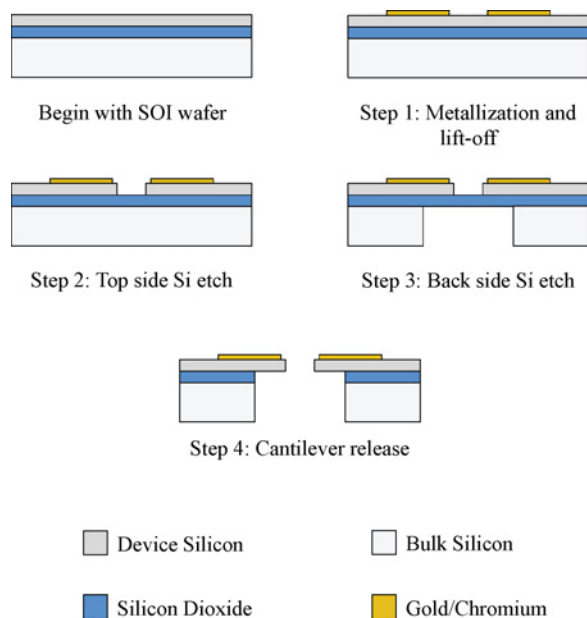


Fig. 9. Fabrication process flow used to produce the electromagnetically transduced microresonators.

The device was placed in the probe station at a pressure setting of  $75 \mu\text{Torr}$  and the device was positioned on the magnet such that the fixed edge of the microcantilever was on the edge of the magnet. Based on results collected with the vibrometer, the quality factor for this device was 7100 and the natural frequency was 51.236 kHz. Note that the difference between the experimentally determined natural frequency and expected natural frequency can be explained by the variation of the thickness of the device layer. The quoted thickness of the device layer was  $2 \pm 0.5 \mu\text{m}$ , but it was observed during fabrication that the thickness was closer to the maximum nominal value, thus if it is assumed that the thickness of the device layer was  $2.5 \mu\text{m}$ , a more accurate estimate of the natural frequency would be 53.378 kHz. The combined resistance of the outer Au/Cr trace with the coaxial cable was  $58 \Omega$ , while the same measurement for the inner loop was approximately  $107 \Omega$ . To approximate how resistively coupled the device was, or in terms of the circuit model, estimate  $R_{Si}$ , the measured resistance between the probes used for the positive excitation and sensing was determined to be  $176 \text{ k}\Omega$ . Note, however, that these resistance values are based on measurements that were conducted immediately after trials were completed and that during trials, these parameters would drift. Specifically, the estimate for  $R_{Si}$  tended to decrease as more trials were conducted. The input waveform was generated using an Agilent 33250A arbitrary waveform generator operated in a high output impedance mode and the response was measured using an SR830 lock-in amplifier. Due to issues with the short term frequency stability of the Agilent 33250A, an Agilent 8648D synthesized signal generator was used as an external 10 MHz reference for the Agilent 33250A. Fig. 11 shows the block diagram of the experimental setup used to perform these electrical measurements. The devices were actuated using the outer current loop. To perform the electrical measurements, the induced EMF from the inner loop was measured using the

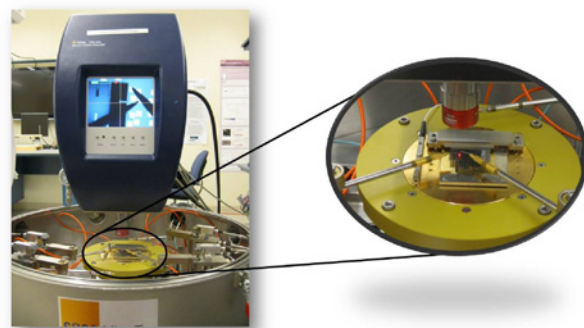


Fig. 10. Part of the experimental setup used to characterize the dynamic response of the electromagnetically transduced microresonators. A Polytec MSA-400 laser Doppler vibrometer was used in conjunction with a Suss Microtec PLV-50 probe station for this purpose. The devices were placed in a permanent magnetic field, in the chamber with a pressure of  $75 \mu\text{Torr}$ .

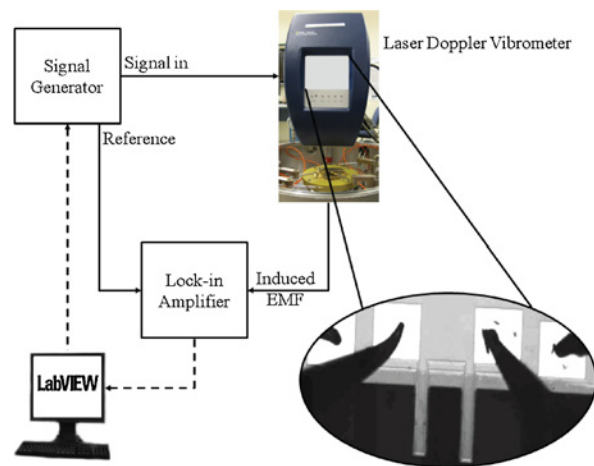


Fig. 11. Block diagram of the electrical setup used to perform electrical measurements on the electromagnetically transduced microresonators.

lock-in amplifier, while for the optical measurements, the output from the LDV was measured using the lock-in amplifier.

As can be extrapolated from the discussion presented in Section III, noise in the input can render significant noise in the output. Primarily due to the inductive coupling between the input and output, high frequency components of noise from the source are not filtered from the response. If the measurement was devoid of noise, the time constant used for the lock-in would be set to filter the response at twice the excitation frequency, which is produced from signal mixing in the lock-in. Based on the excitation frequencies used, this time constant would be on the order of less than a millisecond. Without using the Agilent 8648D as an external reference, time constants greater than 1 s are needed for measurements to have a small standard deviation; however, due to the Agilent 8648D having significantly lower phase noise than the Agilent 33250A, a time constant of 300 ms was used. Since a 12 dB/oct filter slope was used, the recommended dwell time is 7 time constants, to ensure that the measurement settles to within 99% of its final value. A slightly longer than needed dwell time of 3 s was used to guarantee that the dwell time was not an issue with the experiment.



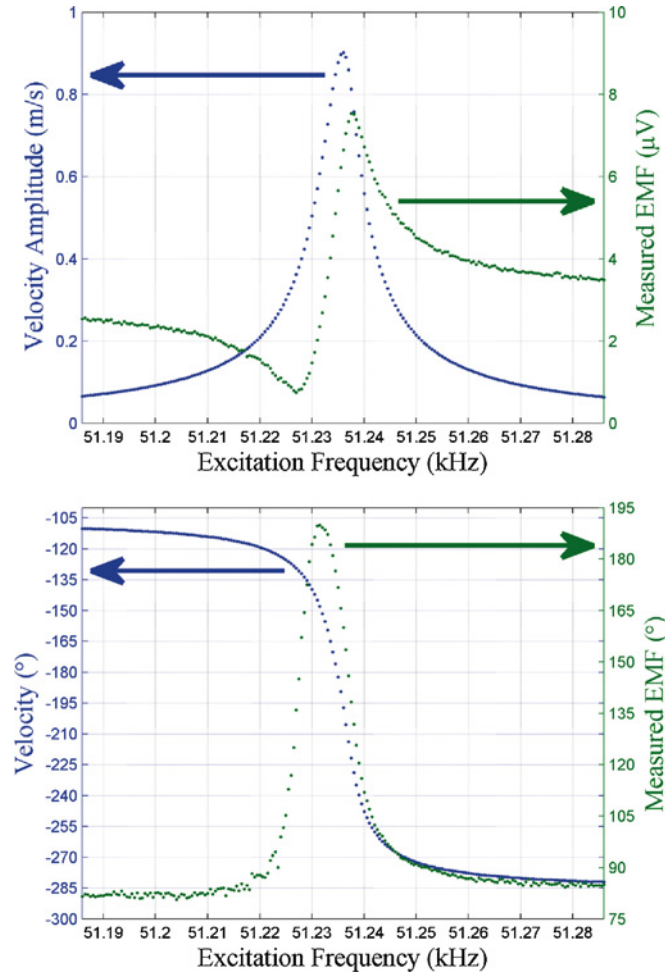


Fig. 12. Frequency response from optical, in blue (left axis), and electrical, in green (right axis), measurements, for an excitation of 20 mVpp. The amplitude of the electrical response demonstrates two effects related to input/output coupling: an effective antiresonance and input voltage biased nonresonant responses. The peak of the electrical response is not commensurate with the optical response due to input/output coupling. The phase of the electrical response shows that the input/output coupling is primarily due to inductive coupling, as the phase of the nonresonant responses more closely approach  $90^\circ$  than  $0^\circ$ .

Fig. 12 depicts a representative experimentally recovered response, obtained optically from the LDV and electrically from the measured EMF, for an excitation level of 20 mVpp. It is evident that the measured electrical response correlates well with the optical response in terms of the natural frequency. However, the recovered electrical response demonstrates effects related to resistive and inductive coupling, such as a nontrivial response away from resonance and the presence of an effective antiresonance. Note that the peak of the electrical response is not commensurate with the optical response due to input/output coupling.

Fig. 13 shows the experimentally recovered electrical responses as a function of excitation amplitude. Excitation voltages of 20, 60, and 100 mVpp are shown in red circles, blue squares, and black diamonds, respectively, and forward and reverse sweeps are denoted with dots and open markers, respectively. The responses clearly show that the resonator vibrates with a higher velocity as the excitation amplitude

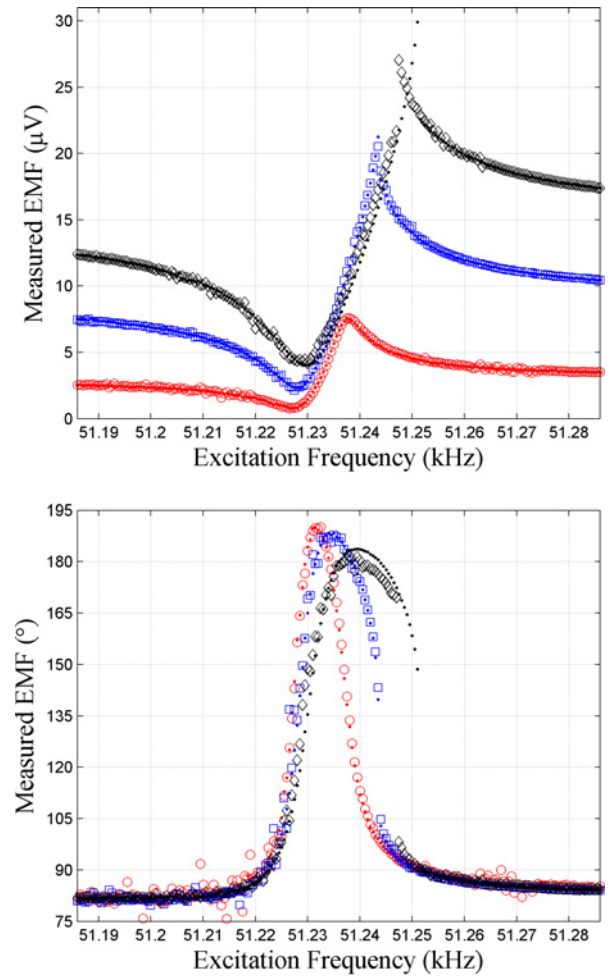


Fig. 13. Amplitude and phase responses from electrical measurements at 20, 60, and 100 mVpp, shown in red circles, blue squares, and black diamonds, respectively. Forward and reverse sweeps are denoted with dots and open markers, respectively. The responses clearly show that the resonator vibrates with a higher amplitude as the excitation amplitude increases. The response also becomes increasingly nonlinear, as is characterized by both the frequency at which the peak amplitude is measured and slope of the phase response near resonance increasing with the excitation amplitude. When the supplied current exceeds the critical current, as is the case at the 100 mVpp excitation, the response shows clear hysteresis with respect to the excitation frequency. Note that even though the mechanical response is characterized as hardening, for some frequencies within the bistable region, the reverse sweep response is greater than the forward sweep response.

increases. Correspondingly, the response becomes increasingly nonlinear as the excitation amplitude increases, which is consistent with the behavior predicted by the model developed in the previous section. When the supplied current exceeds the critical current, as is the case at the 100 mVpp excitation, the response shows clear hysteresis with respect to the excitation frequency. Since the output is strongly coupled to the input via inductive and resistive effects, as predicted in the previous section, for some frequencies within the bistable region, the reverse sweep response is greater than the forward sweep response, even though the mechanical response is characterized as hardening.

As discussed in the previous section, using the reverse polarity configuration can exploit constructive interference effects due to resistive coupling between the input and output

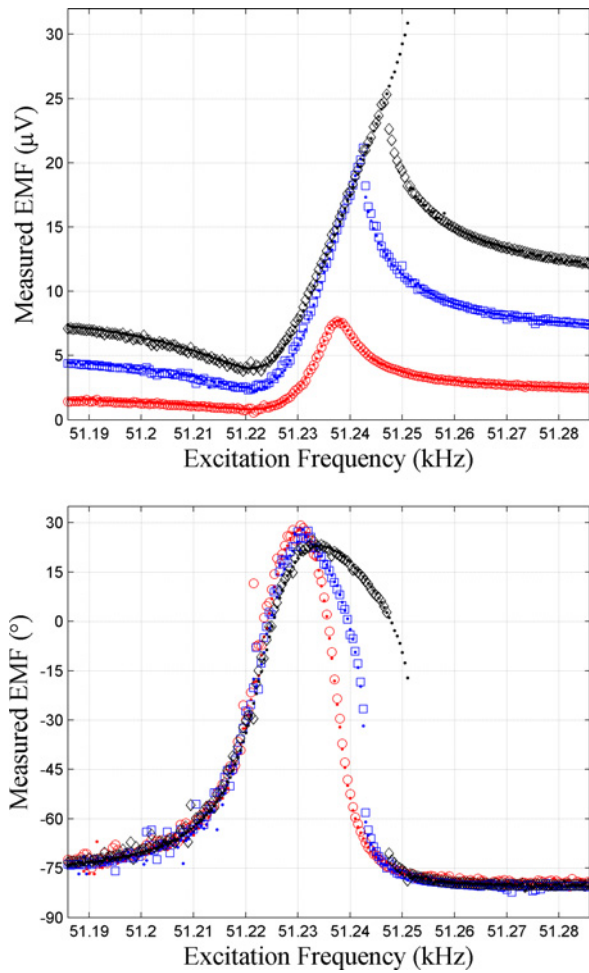


Fig. 14. Amplitude and phase responses from electrical measurements using the reverse polarity configuration, shown using the same convention as in Fig. 13. Due to constructive interference between the induced EMF and the resistive coupling between the input and output, the effects related to an antiresonance are decreased and the response structure more closely resembles a classical hardening response than the response shown in Fig. 13.

for improved signal return and aid in the preservation of the response structure. To be more specific, the response from the reverse polarity configuration more closely resembles a classical hardening response than the standard polarity configuration. Fig. 14 shows the same experiments as Fig. 13, except the polarity of the sensed voltage was reversed. Not only are the effects related to an antiresonance decreased, but the hardening nature of the response structure is preserved. As noted in Section III, the polarity-dependent nature of the response is quite unusual. While the presented experimental results can be explained by the model, it is possible that other unmodeled physics exists, including additional effects attributable to the measurement system or the metal–semiconductor junctions present in the device.

#### A. Parametric Estimation

In order to validate that the presented analytical model for an electromagnetically transduced microcantilever can reproduce the experimentally observed results, parametric estimation was conducted. To do this, a least squared method was employed, where the minimum of the following cost

TABLE III  
AVERAGES OF THE PARAMETER ESTIMATES GENERATED USING A LEAST SQUARED METHOD

Estimated Parameter	Value
$f_n$	51.236 kHz
$Q$	6500
$\kappa_1$	$-1.22 \times 10^{-4}$ V
$\alpha_3$	$4.1 \times 10^{-2}$
$M$	9.24 $\mu$ H
$R_{Si}$	8.1 k $\Omega$

These estimates are for the data shown in Fig. 13.

function was found using a simplex search method (implemented with MATLAB's *fminsearch* algorithm)

$$E = \frac{1}{N} \sum_{i=1}^N |10^6 a_{Ei} e^{i\theta_{Ei}} - 10^6 a_{Mi} e^{i\theta_{Mi}}|^2. \quad (23)$$

Here,  $N$  is the number of data points collected in a given set and  $a_{Ei}$  and  $\theta_{Ei}$  are the experimental estimates for the values  $a_{Mi}$  and  $\theta_{Mi}$  predicted by (22), respectively. Note that the scaling of both the experimental and theoretical values by  $10^6$  was done to account for the magnitude of the response. Also note that this fitting procedure requires good initial guesses for each parameter, as inappropriate guesses may lead to convergence issues. To mitigate this concern, once estimates for the parameters were found, they were randomly perturbed 1000 times to ensure that the estimated parameters were reasonably close to the ones that would be found at the absolute minimum of the cost function. Here, the criteria for reasonably close was that in order to reject the set of estimated parameters, a new set of estimated parameters must decrease the cost function by  $1 \times 10^{-13}$ . Since the estimated natural frequency  $f_n$  was fairly sensitive to poor initial guesses, and a good initial guess for  $f_n$  can be found from a measurement with the vibrometer, its initial guess was only perturbed by up to 0.002%. The remainder of the parameters were randomly varied by 20%.

Overlays of the data shown in Fig. 13 with the frequency response predicted by the analytical model, created using the estimated system parameters, are shown in Fig. 15. The responses generated using the fitted parameters for 20, 60, and 100 mVpp are shown in green upward-pointing triangles, cyan rightward-pointing triangles, and magenta leftward-pointing triangles, respectively, and again forward and reverse sweep responses are shown with dots and open markers, respectively. The parameters used in the model are shown in Table III. These are the averages of the estimates from the six trials shown in Fig. 13. While a very high degree of correlation exists between the analytical and experimental results, it is important to note that there are caveats associated with these estimates.

First, numerical experiments suggest that the least squared method adopted here can provide estimates of the parameters with either a small bias or no bias (i.e., the expected value of a given estimate is very close to the true value). Furthermore, the variance of most of these estimates was small enough that the probability that a given estimate was close to its true value

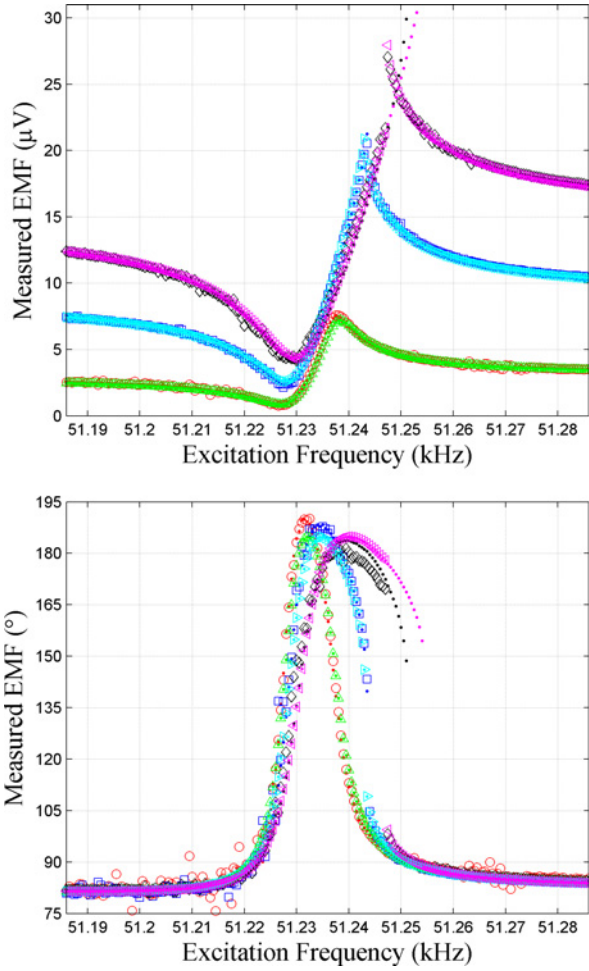


Fig. 15. Overlays of the experimentally recovered amplitude and phase responses shown in Fig. 13 with the response predicted by (22) using the parameters estimated by a least squared method. These estimates are shown in Table III. Responses generated using the estimated parameters for 20, 60, and 100 mVpp are shown in green upward-pointing triangles, cyan rightward-pointing triangles and magenta leftward-pointing triangles, respectively, and again forward and reverse sweep responses are shown with dots and open markers, respectively. Despite the issues with this fitting procedure, which are discussed in the text, and possible parameter drift, these plots provide validation of the presented model.

was quite high. This, however, was not true for  $\alpha_3$  and  $R_{Si}$ . In general, the parameter with the largest relative variance is  $R_{Si}$ , and when the excitation is small, the variance for  $\alpha_3$  is so large that an impractical number of trials are needed to produce a good estimate. This, however, should be expected for  $\alpha_3$  as the influence of nonlinear effects is small when the excitation is small.

The second caveat is that not all of the parameters used in (22) can be uniquely determined. Specifically, in the presence of noise, it is possible to find a set of  $\eta_1$  and  $\kappa_1$  that produce the same response and a set of  $R_{Au/Cr}$  and  $R_{Si}$  that produce the same response. Thus, to produce a single set of parameters,  $\eta_1$  was defined to be

$$\eta_1 = -\kappa_1 \frac{1}{lg\rho (v_0 2\pi f_n)^3} \quad (24)$$

and  $R_{Au/Cr}$  was assumed to be 58  $\Omega$ . The new definition of  $\eta_1$  is consistent with the previous model derivation, however,

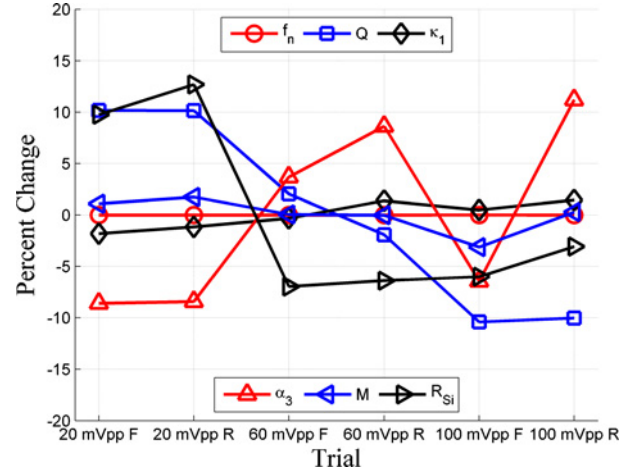


Fig. 16. Plot of the percent differences between the estimate of a given parameter for a given trial relative to the average of the estimates. On the horizontal axis, note that an F after an excitation denotes a forward sweep trial and an R after an excitation denotes a reverse sweep trial. This plot shows that in the presence of noise, the least squares method employed is capable of accurately determining several of the parameters, in particular  $f_n$ . As discussed in the text, this method has issues with determining  $\alpha_3$  for small excitations and in general with  $R_{Si}$ . Due to possible parameter drift during trials, it is not possible to determine if the relative change in  $R_{Si}$  is due to the actual value changing or the fitting procedure. For  $Q$ , however, the relative change in that parameter is most likely due to its value changing slightly during experimentation.

since in experiments the observed natural frequency is greater than the theoretical natural frequency, the thickness  $v_0$  was assumed to be 2.5  $\mu\text{m}$  and the assumed value for  $R_{Au/Cr}$  was based on an experimentally determined value.

The final caveat is that assuming all of the estimates for a given parameter come from the same distribution, provided a large number of estimates are available and that the biases of these estimates are small, the sample mean should be close to the parameter's true value. In this case, only six data sets were used for parameter estimation, and it is unknown if the estimates came from the same distribution. Furthermore, it is unknown how different excitation levels change the distribution of the parameter estimates, and more importantly, there is evidence that suggests some of the parameters drifted during trials. Fig. 16 highlights the percent change in the estimated parameters relative to the average estimates shown in Table III. While the relative change in some of the parameters is insignificant, specifically  $f_n$ , and in some cases can be explained due to the fitting procedure, such as  $\alpha_3$ , the relative change in  $Q$  is most likely due to that parameter changing during experiments. The relative change in  $R_{Si}$  may also be due to the fitting procedure, but it is not possible to rule out that  $R_{Si}$  may also have drifted during trials.

It is important to note that despite the frank issues associated with parametric estimation, the responses for the parameter estimates in Table III closely match the experimentally observed results. In addition, the estimate for the mutual inductance  $M$  is large enough to support the theory that the primary contributions to the mutual inductance are the probe station and contact pads.

## V. CONCLUSION AND FUTURE DIRECTIONS

In this paper, a model to describe the dynamics of an electrically and mechanically isolated electromagnetically actuated microcantilever was developed. The model accounted for the intrinsic coupling between the device's input and output ports, which introduces additional features in the response. Specifically, the inductive and resistive coupling effects introduced an antiresonance and a bias, which significantly alter the dynamics of the device. Experimental results recovered from SOI-based devices validate that the model qualitatively captures the behavior of the device. Current and future research efforts include redesigning the wire loops so as to mitigate or exploit the effects of coupling and noise, modifying the experimental setup such that the parameters  $\eta_1$  and  $\kappa_1$  can be independently estimated and demonstrating the utility of these devices in signal processing applications.

## ACKNOWLEDGMENTS

The authors would like to thank N. D. Sheth and A. Hunkler for their contributions to this work. Any opinions, findings, and conclusions or recommendations expressed in this paper are those of the authors and do not necessarily reflect the views of the National Science Foundation.

## REFERENCES

- [1] K. L. Ekinici, X. M. H. Huang, and M. L. Roukes, "Ultrasensitive nanoelectromechanical mass detection," *Appl. Phys. Lett.*, vol. 84, no. 22, pp. 4469–4471, May 2004.
- [2] D. S. Greywall, B. Yurke, P. A. Busch, A. N. Pargellis, and R. L. Willett, "Evading amplifier noise in nonlinear oscillators," *Phys. Rev. Lett.*, vol. 72, no. 19, pp. 2992–2995, May 1994.
- [3] D. S. Greywall, "Micromechanical RF filters excited by the Lorentz force," *J. Micromech. Microeng.*, vol. 9, no. 1, pp. 78–84, Mar. 1999.
- [4] S. J. Martin, M. A. Butler, J. J. Spates, M. A. Mitchell, and W. K. Schubert, "Flexural plate wave resonator excited with Lorentz forces," *J. Appl. Phys.*, vol. 83, no. 9, pp. 4589–4601, May 1998.
- [5] M. Schiffer, V. Laible, and E. Obermeier, "Design and fabrication of 2D Lorentz force actuated micromirrors," in *Proc. 2002 IEEE/LEOS Int. Conf. Opt. MEMS*, Aug. 2002, pp. 163–164.
- [6] S. C. Jun, X. M. H. Huang, J. Hone, C. A. Zorman, and M. Mehregany, "Evaluation of 3C-SiC nanomechanical resonators using room temperature magnetomotive transduction," in *Proc. IEEE Sens. 2005, 4th IEEE Conf. Sens.*, Oct.–Nov. 2005, pp. 1042–1045.
- [7] X. M. H. Huang, X. L. Feng, C. A. Zorman, M. Mehregany, and M. L. Roukes, "VHF, UHF and microwave frequency nanomechanical resonators," *New J. Phys.*, vol. 7, no. 247, pp. 1–15, Nov. 2005.
- [8] M. J. Thompson, and D. A. Horsley, "Parametrically amplified z-axis Lorentz force magnetometer," *J. Microelectromech. Syst.*, vol. 20, no. 3, pp. 702–710, Jun. 2011.
- [9] M. V. Requa and K. L. Turner, "Electromechanically driven and sensed parametric resonance in silicon microcantilevers," *Appl. Phys. Lett.*, vol. 88, no. 26, p. 263508, Jun. 2006.
- [10] M. V. Requa, "Parametric resonance in microcantilevers for applications in mass sensing," Ph.D. dissertation, Univ. California, Santa Barbara, CA, USA, 2006.
- [11] M. V. Requa, and K. L. Turner, "Precise frequency estimation in a microelectromechanical parametric resonator," *Appl. Phys. Lett.*, vol. 90, no. 17, p. 173508, Apr. 2007.
- [12] J. F. Rhoads, "Exploring and exploiting resonance in coupled and/or nonlinear microelectromechanical oscillators," Ph.D. dissertation, Michigan State Univ, East Lansing, MI, USA, 2007.
- [13] V. Kumar, A. Sabater, and J. F. Rhoads, "Dynamics of coupled electromagnetically-actuated microbeams," in *Proc. 2011 NSF Eng. Res. Innovation Conf.*, 2011.
- [14] D. Paci, F. Pieri, P. Toscano, and A. Nannini, "A CMOS-compatible, magnetically actuated resonator for mass sensing applications," *Sens. Actuators B, Chem.*, vol. 129, no. 1, pp. 10–17, Jan. 2008.
- [15] V. Sazonova, Y. Yaish, H. Ustunel, D. Roundy, T. A. Arias, and P. L. McEuen, "A tunable carbon nanotube electromechanical oscillator," *Nature*, vol. 431, no. 7006, pp. 284–287, Sep. 2004.
- [16] B. Lassagne, D. Garcia-Sanchez, A. Aguasca, and A. Bachold, "Ultrasensitive mass sensing with a nanotube electromechanical resonator," *Nano Lett.*, vol. 8, no. 11, pp. 3735–3738, Nov. 2008.
- [17] A. B. Sabater and J. F. Rhoads, "On the dynamics of two mutually-coupled, electromagnetically-actuated microbeam oscillators," *J. Comput. Nonlinear Dyn.*, vol. 7, no. 3, p. 031011, Jul. 2012.
- [18] M. R. M. Crespo da Silva and C. C. Glynn, "Nonlinear flexural-flexural-torsional dynamics of inextensional beams. I: Equations of motion," *J. Struct. Mech.*, vol. 6, no. 4, pp. 437–448, Jan. 1978.
- [19] S. S. Rao, *Vibration of Continuous Systems*. New York, NY, USA: Wiley, 2007.
- [20] A. H. Nayfeh and D. T. Mook, *Nonlinear Oscillations*. New York, NY, USA: Wiley-Interscience, 1995.
- [21] C. R. Paul, *Inductance: Loop and Partial*. New York, NY, USA: Wiley-IEEE, 2010.
- [22] J. R. Long, "Monolithic transformers for silicon RF IC design," *IEEE J. Solid-State Circuits*, vol. 35, no. 9, pp. 1368–1382, Sep. 2000.
- [23] N. Fong, J.-O. Plouchart, N. Zamdmer, J. Kim, K. Jenkins, C. Plett, and G. Tarr, "High-performance and area-efficient stacked transformers for RF CMOS integrated circuits," in *Proc. 2003 IEEE MTT-S Int. Microwave Symp.*, Jun. 2003, pp. 967–970.
- [24] A. B. Sabater, V. Kumar, A. Mahmood, and J. F. Rhoads, "On the nonlinear dynamics of electromagnetically-transduced microresonators," in *Proc. 2011 ASME Int. Des. Eng. Tech. Conf., Comput. Inform. Eng. Conf.*, 2012, p. DETC 2012-70648.



**Andrew B. Sabater** received the B.S. degree in general engineering with distinction from Harvey Mudd College, Claremont, CA, USA, in 2009.

He is currently a Graduate Research Assistant at Purdue University, West Lafayette, IN, USA. His current research includes the predictive design, testing, and analysis of isolated and coupled resonant microelectromechanical systems, with applications in chemical and biological sensing, electromechanical signal processing, and timing.



**Vijay Kumar** received the B.S. degree in mechanical engineering from Anna University, Chennai, India, in 2007, and the M.S. and Ph.D. degrees in mechanical engineering from Purdue University, West Lafayette, IN, USA, in 2010 and 2011, respectively.

His current research interests include the predictive design, analysis, and implementation of resonant micro/nanoelectromechanical systems for use in chemical and biological sensing; the dynamics of parametrically excited systems; and the behavior of electromechanical systems operating in rich multiphysics environments.

Dr. Kumar is a Student Member of the American Society of Mechanical Engineers and was a 2010 recipient of Purdue University's Ward A. Lambert Teaching Fellowship.



**Aamer Mahmood** (M'07) received the B.E. degree in electrical engineering with honors from the N.W.F.P. University of Engineering and Technology, Peshawar, Pakistan, in 1992. He received the M.S. degree in electrical engineering from the University of Engineering and Technology, Lahore, Pakistan, in 1999. He received the Ph.D. degree in electrical engineering from the University of Texas at Arlington, Arlington, TX, USA, in 2006.

He was a Post-Doctoral Researcher with the School of Electrical and Computer Engineering, Pur-

due University, West Lafayette, IN, USA, from 2006 to 2008. He has been with the Birck Nanotechnology Center, Purdue University, as a Research Engineer since 2008. He was promoted to the ranks of a Research Scientist and Senior Process Scientist in 2011 and 2012, respectively. His current research includes the development of novel microsensors and actuators in diverse areas like biomedical engineering, fluid flow in porous media, and radiation detection. He has published over 20 articles in journals and conference proceedings.



**Jeffrey F. Rhoads** received the B.S., M.S., and Ph.D. degrees in mechanical engineering from Michigan State University, East Lansing, MI, USA, in 2002, 2004, and 2007, respectively.

He is currently an Associate Professor in the School of Mechanical Engineering, Purdue University, West Lafayette, IN, USA, where he is affiliated with both the Birck Nanotechnology Center and Ray W. Herrick Laboratories. His current research interests include the predictive design, analysis, and implementation of resonant micro/nanoelectromechanical systems for use in chemical and biological sensing, electromechanical signal processing, and computing; the dynamics of parametrically excited systems and coupled oscillators; and the behavior of electromechanical systems operating in rich multiphysics environments.

Dr. Rhoads is a member of the American Society for Engineering Education (ASEE) and the American Society of Mechanical Engineers (ASME), where he serves on the Student Design Committee and the Design Engineering Division's Technical Committees on Micro/Nanosystems and Vibration and Sound. He was a 2009 recipient of the National Science Foundation's Faculty Early Career Development (CAREER) Award and the Purdue University School of Mechanical Engineering's Harry L. Solberg Best Teacher Award, and was a 2011 recipient of the ASEE Mechanics Division's Ferdinand P. Beer and E. Russell Johnston, Jr. Outstanding New Mechanics Educator Award.